

Supplement of Biogeosciences, 13, 27–44, 2016
<http://www.biogeosciences.net/13/27/2016/>
doi:10.5194/bg-13-27-2016-supplement
© Author(s) 2016. CC Attribution 3.0 License.



Biogeosciences  Open Access

Supplement of

Detection and spatiotemporal analysis of methane ebullition on thermokarst lake ice using high-resolution optical aerial imagery

P. R. Lindgren et al.

Correspondence to: P. R. Lindgren (pregmi@alaska.edu)

The copyright of individual parts of the supplement might differ from the CC-BY 3.0 licence.

Sect. S1. Principal Component Analysis

Multi-spectral remote sensing data consists of high inter-band correlation and therefore bands within a dataset carry redundant information (Rocchini et al., 2007). Principal Component Analysis (PCA) transforms a set of correlated variables in original image bands into a set of linearly uncorrelated orthogonal components (principal components) (Schowengerdt, 2007; Estronell et al., 2013). It reduces the dimensionality of the data and outputs the maximum amount of information with a physical meaning from the original bands into the least number of principal components (Estronell et al., 2013). After transformation, the first principal component has the variables that account for the most variance in the dataset and each succeeding independent component in turn carries less and less of the original data variance.

Sect. S2. Image segmentation and classification to map bubble patches on lake ice image

Based on empirical performance tests, we used the first two PCA components (PC 1 and PC 2) to perform multi-resolution segmentation embedded in eCognition Developer™ software to create image objects (eCognition Developer 7 Reference, 2007a). The advantage of using multi-resolution segmentation is that it allows to create objects of different scales while minimizing the heterogeneity within the resulting object at the given scale (Baatz and Schape, 2000). For example, we applied a large-scale factor to create large objects of different lake ice characteristics and a small-scale factor to create small bubble patch objects. We performed region-specific classification for the identification of target features within the domain of that particular region. In general, for classification we used spectral characteristics in PC bands 1 and 2, contextual information pertaining to image objects such as an image object's relationship with its neighbors and sub- and super-objects, a Canny edge detection algorithm (Canny, 1986; eCognition Developer 7 Reference, 2007b) and morphological filters available in the eCognition Developer™ software.

The classification method performed very well in identifying bubble patches (Fig. 2) with an overall accuracy of 98% when compared to manually identified bubble features in image segments that served as our ground truth sample data for classification accuracy assessment.

Due to thin lake ice condition on image acquisition days, it was not feasible to collect ground truth data of ebullition bubble patches for the purpose of accuracy assessment. It is important to note we did not check our classification accuracy in terms of object's geometry or boundary delineation. We only performed quantitative site-specific accuracy assessment using error matrix that only checks the agreement of object classes between manually classified reference sample and object-based classification results.

Sect. S3. Classification of bubble patches based on size

The Maximum Likelihood Classification (MLC) was a pixel-based classification that categorized bubble patches based on the pixel spectral characteristics. Therefore, the pixels within an extended bubble patches may be assigned to more than one seep class (multi-type bubble patch) depending on the variation of brightness values within the patch. Since the size of bubble patches is also an additional important indicator of seep class and methane flux (Walter Anthony et al., 2010), in a subsequent step we further investigated the size of each seep class in a multi-type bubble patch identified by MLC. Based on the highest flux seep type and its size in a patch, we re-assigned bubble patches to a more accurate methane flux. For example, a bubble patch with a combination of C-, B- and A-type seep, C-type is the highest flux seep. Thus, we checked the total area of C-type seep. The whole bubble patch was classified as C-type seep only if the area of C-type seep was greater than 0.04 m² otherwise it was classified as B-type seep (Table S1). The thresholds on size are based on seep morphology described by Walter Anthony et al., 2010 and our field observations.

References

- Baatz, M. and Schäpe, A.: Multiresolution segmentation – an optimization approach for high quality multi-scale image segmentation, *Angewandte Geographische Informationsverarbeitung XII, Beiträge zum AGIT-Symposium Salzburg 2000*, Herbert Wichmann Verlag, Karlsruhe, 12–23, 2000.
- Canny, J.: A computational approach to edge detection, *IEEE T. Pattern Anal.*, 8, 679–714, 1986.

Definiens, Segmentation Algorithms In Definiens Developer 7 Reference Book, Document Version 7.0.0.843, 15–27, Definiens AG, München, Germany, 2007a.

Definiens, Edge Extraction Canny In Definiens Developer 7 Reference Book, Document Version 7.0.0.843, 62–63, Definiens AG, München, Germany, 2007b

Estornell, J., Marti-Gavila, J. M., Teresa Sebastia, M., and Mengua, J.: Principal component analysis applied to remote sensing, *Modelling in Science Education and Learning*, 6, 83–89, 2013.

Rocchini, D., Ricotta, C., and Chiarucci, A.: Using satellite imagery to assess plant species richness: The role of multispectral systems, *Appl. Veg. Sci.*, 10, 325–332, 2007.

Schowengerdt, A.: *Principal Components In Remote sensing: Models and methods for image processing*, Third Edn., Academic Press, San Diego, CA, 193–199, 2007.

Walter Anthony, K., Vas, D. A., Brosius, L., Chapin III, F. S., and Zimov, S. A.: Estimating methane emissions from northern lakes using ice- bubble surveys, *Limnol. Oceanogr.-Meth.*, 8, 592–609, 2010.

Table S1. Conditions applied to classify bubble patches that are identified to have multiple seeps (multi-type bubble patch) by MLC. A single final seep type is assigned to the multi-type bubble patch based on the size of the highest flux seep that is present in the patch.

		Highest flux seep in the bubble patch							
		Hotspot		C-type seep		B-type seep			
If area (m ²)		< 0.04	0.04 >=	< 0.09	>= 0.09	< 0.04	>= 0.09	< 0.01	0.01
Assign class		B-type	C-type	Hotspot	B-type	C-type	A-type	B-type	

Table S2. Tukey’s Honestly Significant Difference (HSD) test showing significant difference (with p-values* < 0.05) between bubble patches identified in aerial images as C- and A- type seeps, Hotspot and A-type seeps, and Hotspot and B-type seeps for 2011 and 2012.

Year 2011

95 % Confidence Interval				
Seeps	Mean Difference	Lower Bound	Upper Bound	p-values
B-A	-6.43	-18.89	6.03	0.54
C-A *	-20.28	-37.14	-3.40	0.01*
Hotspot-A *	-32.73	-41.85	-23.61	0*
C-B	-13.84	-32.32	4.63	0.21
Hotspot-B *	-26.30	-38.13	-14.48	0.00*
Hotspot-C	-12.45	-28.87	3.95	0.21

Year 2012

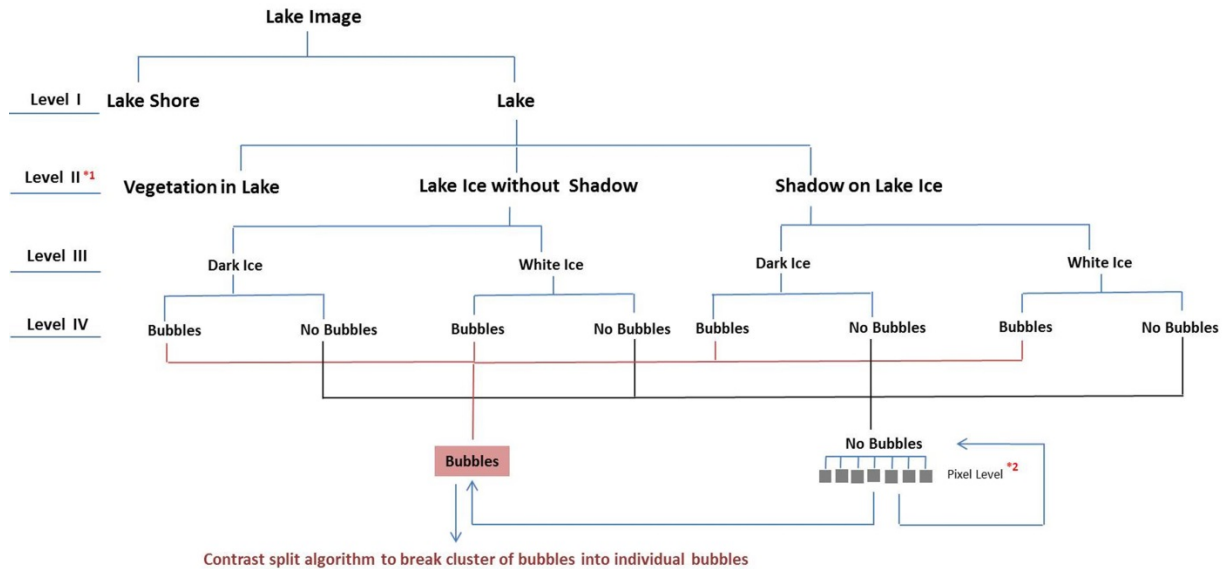
95 % Confidence Interval				
Seeps	Mean Difference	Lower Bound	Upper Bound	p-values
B-A	-6.41	-12.95	0.13	0.06
C-A *	-15.36	-23.84	-6.88	0.00*
Hotspot-A *	-13.51	-17.98	-9.05	0.00*
C-B	-8.95	-18.67	0.78	0.08

Hotspot-B*	-7.10	-13.62	-0.58	0.02*
Hotspot-C	1.85	-6.62	10.31	0.94

Table S3: Accuracy assessment table for bubble patch classification

Seep Class	Year	Producer's Accuracy (%)	Omission Error (%)	Commission Error (%)	User's Accuracy (%)	Overall Accuracy
A-type	2011	50.00	50.00	38.46	61.54	38.10
	2012	52.54	47.46	6.06	93.94	50.82
B-type	2011	71.43	28.57	61.54	38.46	33.33
	2012	63.64	36.36	70.21	29.79	25.45
C-type	2011	33.33	66.67	75.00	25.00	16.67
	2012	10.00	90.00	92.86	7.14	4.35
Hotspot	2011	45.83	54.17	8.33	91.67	44.00
	2012	67.50	32.50	27.03	72.97	54.00

Figure S1. Image object hierarchy used in the objected oriented classification technique developed to identify bubble patches on early winter lake ice. Image segmentation is performed in each level and image objects are classified. In the first level, segmentation is performed on the whole lake image to identify Lake Shore and Lake. In the second level, only the Lake region is segmented and image objects derived from the Lake are classified into different lake ice characteristics. This process continues as it proceeds towards lower and finer classification levels until Bubbles are identified in the lake ice.



*1 : The number of image object class (lake ice type) may be less or more depending on lake ice conditions across images.
 *2 : Check if any bright pixel that should be a part of bubble object is still missing. If there is any then assign that pixel as 'Bubbles'.

Figure S2. (a) and (b) are 2011 bubble patch maps of Goldstream L. overlaid on Principal Component 1 image (PC 1) and inverted PC 1. Inverted PC 1 is calculated using the formula $\text{Inverted PC 1} = 255 + (\text{PC 1} * (-1))$. The land around lake is shown in true color composite of red, green and blue bands (RGB); (c) and (d) show the area highlighted in the black box in (a) overlaid on RGB composite and PC 1 respectively. Bubble patches appear bright in RGB whereas they appear dark in PC 1. A rectangular wooden instrument platform in the center of the lake (blue box) as well as clusters of lily pads (one example highlighted in green box) on the northern and south-western parts of the lake (see Fig. 1) also appear dark on PC 1. Therefore, we inverted PC 1 to retain their original brightness characteristic, i.e. appear bright against background lake ice. This is shown in e.

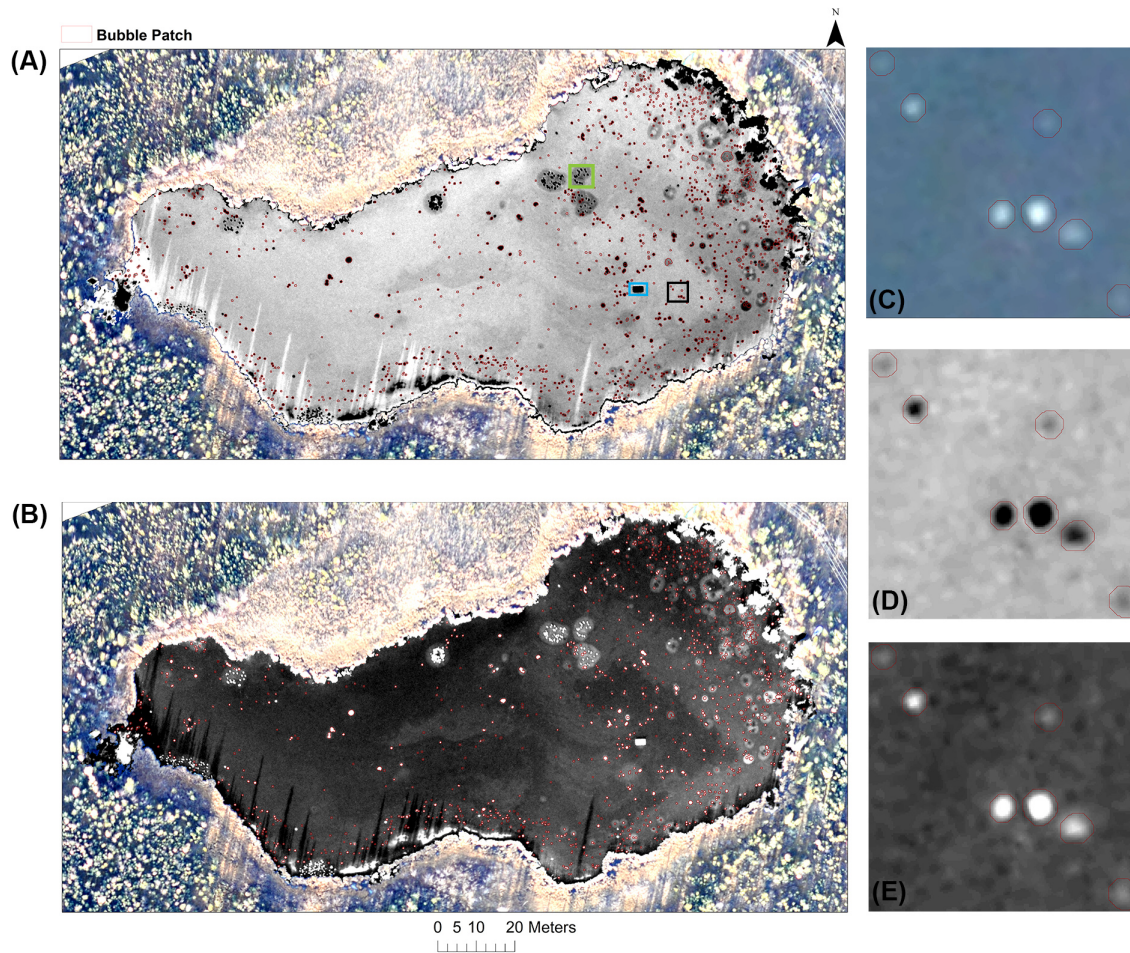


Figure S3. Photo of an ice block cross-section in April of 2013 from an ebullition seep on Goldstream L., Fairbanks, Alaska. The bubble size variation traces dynamics of the point source emission during winter. Vertically-oriented, circular and flat layers of methane bubbles separated by clear ice indicate highly episodic nature of ebullition. Varying size of bubbles and periods of ice growth with no bubbling confirm previous bubble-trap observations that bubbling is episodic rather than constant over time. Black marks on the ruler have 10-cm spacing.

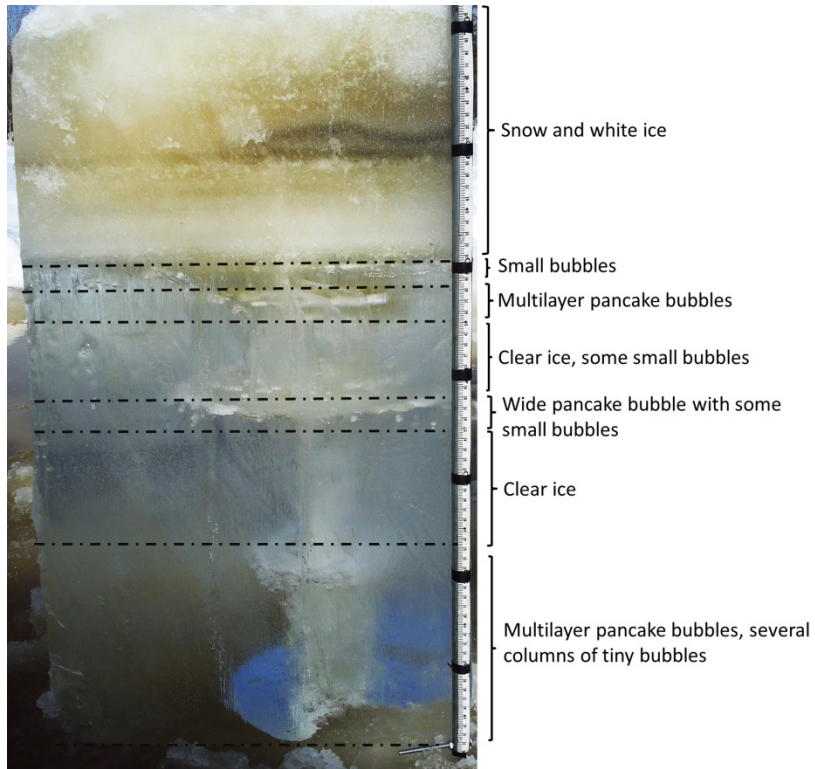


Figure S4. Ice-free Hotspot location map of Goldstream L. overlaid on a natural color composite (red, green and blue bands) image acquired using a UAV on 14 October, 2012.

